



Delft University of Technology

## On the flow organization of a chevron synthetic jet

Crispo, Cuono Massimo; Greco, Carlo; Avallone, Francesco; Cardone, G

### DOI

[10.1016/j.expthermflusci.2016.11.009](https://doi.org/10.1016/j.expthermflusci.2016.11.009)

### Publication date

2017

### Document Version

Final published version

### Published in

Experimental Thermal and Fluid Science

### Citation (APA)

Crispo, C. M., Greco, C., Avallone, F., & Cardone, G. (2017). On the flow organization of a chevron synthetic jet. *Experimental Thermal and Fluid Science*, 82(4), 132-146.  
<https://doi.org/10.1016/j.expthermflusci.2016.11.009>

### Important note

To cite this publication, please use the final published version (if applicable).  
Please check the document version above.

### Copyright

Other than for strictly personal use, it is not permitted to download, forward or distribute the text or part of it, without the consent of the author(s) and/or copyright holder(s), unless the work is under an open content license such as Creative Commons.

### Takedown policy

Please contact us and provide details if you believe this document breaches copyrights.  
We will remove access to the work immediately and investigate your claim.



## On the flow organization of a chevron synthetic jet



C.M. Crispo<sup>a,\*</sup>, C.S. Greco<sup>a</sup>, F. Avallone<sup>b</sup>, G. Cardone<sup>a</sup>

<sup>a</sup> Dept. of Industrial Engineering, University of Naples Federico II, Via Claudio 21, 80125 Naples, Italy

<sup>b</sup> AWEF Dept., Delft University of Technology, Kluyverweg 1, 2629 HS Delft, The Netherlands

### ARTICLE INFO

#### Article history:

Received 25 July 2016

Received in revised form 10 November 2016

Accepted 10 November 2016

Available online 11 November 2016

#### Keywords:

Synthetic jets

Chevron nozzle

Vortex ring

Stereoscopic particle image velocimetry

### ABSTRACT

In the present study, the flow fields generated by two synthetic jets with a chevron and a conventional circular nozzle exits are studied and compared. For both configurations, the devices are operated at the same input electrical power, thus leading to Reynolds and Strouhal numbers equal to 5600 and 0.115 (for the circular exit) and 6000 and 0.106 (for the chevron exit). Phase-locked stereoscopic particle image velocimetry measurements are used to reconstruct the three-dimensional coherent vortex structures. Time-averaged and phase-averaged mean and turbulent statistics are analysed and discussed. The flow field strongly depends on the exit geometry. In presence of the chevron exit, the conventional vortex ring issued through the circular nozzle exit, is replaced by a non-circular vortex ring with additional streamwise vortices. The mutual interaction between these structures prevents the axis-switching of the non-circular vortex ring during its convection. These streamwise vortices disappear convecting downstream and the vortex ring assumes a circular shape. Comparing the two configurations, the chevron exit generates a larger time-averaged streamwise velocity along the centreline but with lower turbulent kinetic energy intensity. Differences are also present between the notch and the apex planes of the chevron exit. In the notch plane, both the time-averaged axial velocity component profile in the spanwise direction and the shear layer width are wider than in the apex plane. Furthermore, the presence of the streamwise vortices causes a flow motion towards the jet axis in the apex plane and an opposite motion in the notch plane.

© 2016 Elsevier Inc. All rights reserved.

### 1. Introduction

Synthetic-jets actuators, also called zero-net-mass-flux actuators, are promising devices used in the fields of flow control [1–5] and heat transfer enhancement [6–10]. These devices are made by a cavity bounded by an oscillating membrane, and by an orifice plate. They transfer momentum from the oscillating membrane to the fluid in which they are embedded, without the need of active mass injection. For this reason, such jets are widely used in lowcost and lowspace applications. Furthermore, they can be easily designed by using a lumped method [11–13].

Synthetic jets are characterized by an ejection and a suction phase. During the former, a slug of fluid, necessary to synthesize the jet, is ejected through the same opening used as inlet during the suction stage. More in detail, the momentum transferred to the fluid inside the cavity has to be large enough to overcome the suction forces associated with the ingestion stroke and the effect of the exit geometry [14]. A formation criterion was proposed by Holman et al. [14] for round and slot orifices. If the forma-

tion criterion is satisfied a train of vortex rings, generated along the shear layer that rolls up at the nozzle exit edge, convects away from the exit generating a steady turbulent jet. Under certain particular conditions, each vortex ring may be followed by a column of fluid called trailing jet. The existence and extension of the trailing jet depend on the Strouhal number [15]. The Strouhal number and the Reynolds number are the dimensionless parameters which govern the synthetic jet flow field. They are defined as follows:

$$Sr = D/L_0 = fD/U_0 \quad (1)$$

$$Re = \rho U_0 D / \mu \quad (2)$$

where  $U_0$  is the characteristic velocity of the jet,  $D$  is the characteristic length,  $f$  is the oscillating frequency of the membrane,  $\rho$  is the fluid density,  $\mu$  is the fluid dynamic viscosity and  $L_0$  is the stroke length (defined as  $U_0/f$ ). According to Smith and Glezer [16], the reference velocity  $U_0$  is defined as  $U_0 = \frac{1}{\tau} \int_0^{\tau/2} u_e(t) dt$ , where  $\tau$  is the actuation period and  $u_e$  is the velocity along the jet centreline at the exit section.

A general approach to characterize synthetic jets is to compare the flow field with an equivalent continuous jet at the same Rey-

\* Corresponding author.

E-mail address: [cuonomassimo.crispo@unina.it](mailto:cuonomassimo.crispo@unina.it) (C.M. Crispo).



nozzle may lead to an early breakup of the train of vortex rings preventing the generation of the synthetic jet. For this reason, in the present work, stereoscopic PIV measurements of the flow field generated by a chevron synthetic jet are carried out. The jet formation and its evolution are studied. The flow field is then compared with that of an equivalent circular synthetic jet, operated at the same input electrical power.

## 2. Experimental set-up and data reduction technique

### 2.1. Experimental set-up

Experiments are carried out on two synthetic jet devices with a circular and a chevron nozzle exit (Fig. 1). In order to generate the synthetic jet, the contoured nozzle is coupled with a loudspeaker (Audiola SBL 20N BL) of diameter equal to 100 mm (Fig. 1a). The contoured nozzle and the chevron cap used in this work are detailed described in Violato and Scarano [25] and Violato et al. [21]. The round nozzle has an exit diameter ( $D$ ) of 10 mm, it is 125 mm long and it has a contraction ratio of 56:1. The chevron synthetic jet is realized by applying a chevron exit cap (Fig. 1b) on top of the round nozzle. The chevron exit has six chevron elements 4.5 mm high and inclined towards the jet axis of  $18.2^\circ$ , thus resulting in a penetration depth of 1.48 mm.

The resonance frequency of the system in both configurations is experimentally determined by measuring the loudspeaker impedance. The system is characterized by two resonance frequencies equal to about 80 Hz and 300 Hz. The loudspeaker is driven by a sinusoidal input signal with a frequency of 96 Hz by a Diligent Inc. Analog Discovery<sup>®</sup> coupled with an amplifier. At this working frequency the impedance of the two synthetic jet configurations differs of less than 1.5%. The system is operated with electrical power equal to 5.2 W. Under these operating conditions, the Reynolds number (Eq. (1)) is equal to 5600 and 6000 and the Strouhal number (Eq. (2)) is equal to 0.115 and 0.106 for the circular and the chevron configurations, respectively. They are estimated by measuring the axial velocity component along the jet centreline at  $0.6 D$  from the nozzle exit, which is the closest point to the exit plane of the round nozzle in the field of view (FOV).

The origin of reference system is fixed at the centre of the round nozzle exit section. The  $x$ -axis is aligned with the jet centreline and the  $y$ - and  $z$ -axes lie in the plane perpendicular to the  $x$ -direction,

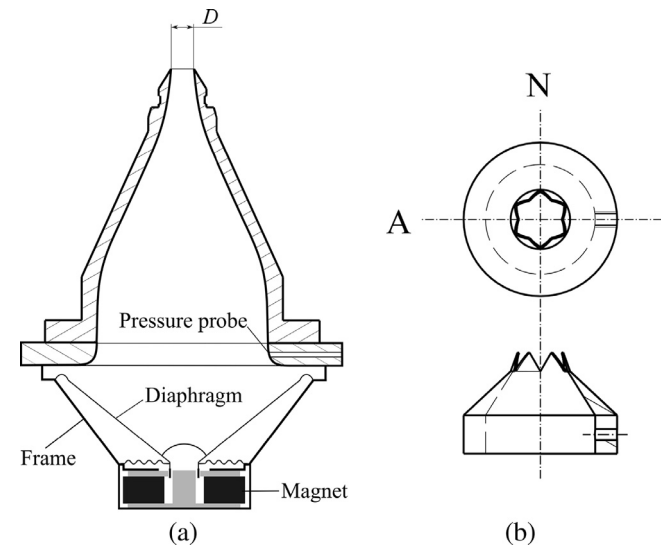


Fig. 1. Synthetic jet device: (a) sketch of the jet device and (b) of the chevron cap.

forming a clockwise reference system. A sketch of the adopted reference system is reported in Fig. 2.

### 2.2. PIV measurements

Stereoscopic particle image velocimetry (Stereo-PIV) [26] is used to measure the instantaneous two-dimensional (2D) three-component (3C) velocity field. Particle images are acquired in the  $x$ - $y$  plane passing through the jet axis. In presence of the chevron exit,  $x$ - $y$  planes including both the apex (A, Fig. 1b) and notch (N, Fig. 1b) are investigated.

Furthermore, phase-locked scanning Stereo-PIV measurements are carried out in order to reconstruct the three-dimensional (3D) coherent vortex structures. The 3D reconstruction is carried out recording particle images in the crosswise  $y$ - $z$  plane as follows: for a given phase the position of the vortex core cross-section is detected by looking at the streamwise measurements. Then, the synthetic jet device is placed with the  $x$ -axis perpendicular to the laser sheet, on a slide with micrometre accuracy and the flow field is scanned along the  $x$ -direction with 33 equidistant planes across the vortex core (Fig. 2b). The distance between two subsequent planes is set to  $\Delta x = 0.5$  mm. For each plane 500 double frame particle images are acquired. Three phases are investigated corresponding to a vortex ring position at about  $x/D = 1.75, 3$  and  $4.5$ .

Oil droplets with a diameter of approximately  $1 \mu\text{m}$  are used to seed the flow. Illumination is provided by the Quantel Evergreen laser that is a double pulsed Nd:YAG laser (532 nm, 200 mJ per pulse,  $<10$  ns pulse duration). The time separation between the two laser pulses is set to  $\Delta t = 8 \mu\text{s}$  and to  $\Delta t = 6 \mu\text{s}$  for the streamwise and the crosswise plane, respectively. The laser sheet thickness is about 1 mm. Particle images are recorded by two Andor Zyla sCMOS cameras ( $2160 \times 2560$  pixels, 16 bit,  $6.5 \mu\text{m}$  per pixel) equipped with Schempflug adapters and Tokina 100 mm focal length objectives set at numerical aperture  $f_{\#} = 16$ . The resulting digital resolution is 50 pixels/mm. The measurement domain in

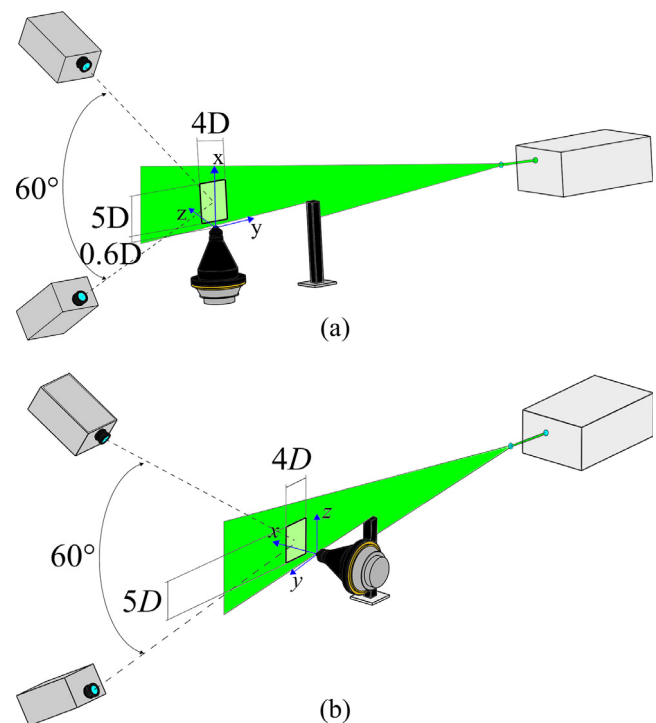


Fig. 2. Sketch of the experimental set-up: Stereo-PIV system and measurement domain for (a) streamwise and (b) crosswise measurement planes.

the  $x$ - $y$  plane (Fig. 2a) ranges between  $0.6 < x/D < 5.6$  and  $-2 < y/D < 2$ , while in the crosswise  $y$ - $z$  plane (Fig. 2b) ranges between  $-2 < y/D < 2$  and  $-2.8 < z/D < 2.2$ . The acquisition system is synchronized with the synthetic jet in order to perform phase-locked measurements. The synchronization is realized by using a Digilent Inc. Analog Discovery®. The input signal to the loudspeaker is used also as trigger for the acquisition system. The acquisition is performed at the frequency  $f_2$  estimated following Greco et al. [27]. The phenomenon is sampled with a  $12^\circ$  phase separation. In order to obtain reliable turbulent statistics, 15,000 double frame particles images (500 for each phase) are recorded.

A multi-pass algorithm with windows deformation and Blackman weighting windows [28–31] is used to compute the velocity fields. The final interrogation window size is  $32 \times 32$  pixels with an overlap of 75%, thus resulting in a vector pitch of 0.16 mm (approximately 62 vectors per  $D$ ) for the streamwise measurements. Differently, for the crosswise measurements the final interrogation window size is  $24 \times 24$  pixels with an overlap of 75% and vector pitch of 0.12 mm (approximately 83 vectors per  $D$ ). A normalized median validation criterion [32] is applied to remove spuriously detected vectors. The uncertainty in displacement, related to the peak localization, is the main contribution to velocity uncertainty. For the given particle size (approximately 3 pixels), image noise and particle displacement, the random error is found to be approximately 2% of the instantaneous velocity in the jet core.

### 2.3. Data reduction

The velocity triple decomposition scheme [33] is used for the data analysis:

$$u_i(\mathbf{x}, t) = U_i(\mathbf{x}) + \tilde{u}_i(\mathbf{x}, t) + u'_i(\mathbf{x}, t) \quad (3)$$

where  $u_i$  is the  $i$ -th instantaneous velocity component ( $u_1 = u$ ,  $u_2 = v$ ,  $u_3 = w$ ),  $\mathbf{x} = (x, y, z)$ ,  $U_i$  is the time-averaged velocity component,  $\tilde{u}_i$  is the phase-correlated velocity component and  $u'_i$  is the turbulent fluctuations. They are defined as follows:

$$U_i(\mathbf{x}) = \lim_{T \rightarrow \infty} \frac{1}{T} \int_0^T u_i(\mathbf{x}, t) dt \quad (4)$$

$$\langle u_i(\mathbf{x}, t) \rangle = \lim_{N \rightarrow \infty} \frac{1}{N} \sum_{k=0}^N u_i(\mathbf{x}, t + k\tau) \quad (5)$$

$$\tilde{u}_i(\mathbf{x}, t) = \langle u_i(\mathbf{x}, t) \rangle - U_i(\mathbf{x}) \quad (6)$$

$$u'_i(\mathbf{x}, t) = u_i(\mathbf{x}, t) - \langle u_i(\mathbf{x}, t) \rangle \quad (7)$$

where  $u_i(\mathbf{x}, t)$  is the phase-averaged velocity component,  $N$  is the number of the instantaneous fields at the same phase,  $k$  is an integer and  $\tau$  is the time period of the wave produced by the loudspeaker.

The time-averaged (TKE) and the phase averaged ( $\langle TKE \rangle$ ) turbulent kinetic energy can be computed as

$$TKE = \sum_i \overline{u'_i u'_i} / 2 \quad (8)$$

$$\langle TKE \rangle = \sum_i \langle u'_i u'_i \rangle / 2 \quad (9)$$

where  $\overline{u'_i u'_i}$  and  $\langle u'_i u'_i \rangle$  are the time-averaged and phase-averaged Reynolds stresses, respectively.

## 3. Results

In this section, the mean and statistical flow fields generated by both the circular and chevron synthetic jets are discussed and compared. Since it has been experimentally proved that the flow fields in the  $x$ - $y$  plane are symmetric with respect to the jet centreline, data are further averaged using the two mid-planes and then mirrored for easy of interpretation. As a consequence, measurements noise is further reduced.

In the following, the starting phase  $\phi = 0^\circ$  is considered as the phase corresponding to the first positive axial-velocity value measured along the jet axis at the most upstream location.

### 3.1. Time-averaged velocity field

In Fig. 3, the streamwise evolution of the time-averaged axial velocity component along the jet centreline ( $U_c$ ) is shown. The figure shows different behaviours of the two devices. More in detail, for the chevron synthetic jet  $U_c$  increases faster than the for the circular jet and it attains its maximum  $0.4 D$  more downstream ( $x/D = 2.3$ ). In the decay region, the jet with the chevron exit exhibits higher  $U_c$ . Furthermore, for the circular synthetic jet  $U_c$  decreases with  $x^{-1}$  in agreement with the findings of Cater and Soria [17] and Mallinson et al. [34] while the chevron one decreases with  $x^{-0.55}$ .

The mean flow field topology is further discussed by looking at evolution of the time-averaged axial velocity ( $U$  profiles in the  $y$ -direction, Fig. 4). At  $x/D = 0.6$  the circular device (Fig. 4a) shows a region of constant  $U$  across the jet centreline ( $-0.3 < y/D < 0.3$ ). Furthermore, it shows a change of slope at  $y/D = \pm 0.65$  because of the long permanence of the vortex ring near the nozzle exit during the ejection phase, as will be shown in the following Section 3.2. Moving away from the centreline, a region of negative  $U$  is measured. It is due to the suction phase which affects the flow field up to  $x/D = 2$ . Moving downstream, the  $U$  profile shows a bell-shaped distribution. For  $x/D \geq 2$ , the maximum of  $U$  along the jet axis decreases ( $U_c$  in Fig. 3) and the jet spreads because of the radial momentum diffusion [35].

The chevron exit geometry acts as an additional converging nozzle in the apex plane. As a consequence, at  $x/D = 0.6$  (see Fig. 4b), the width of the  $U$  profile is smaller than in presence of the circular exit. Moreover, two small peaks at  $y/D = \pm 0.2$  are measured. At this streamwise position, regions with negative  $U$  are present at  $-1.29 < y/D < -0.74$  and  $0.74 < y/D < 1.29$ , and similarly to the circular configuration, the velocity decays to zero changing its slope. Moving downstream ( $x/D \geq 2$ ), the two small peaks

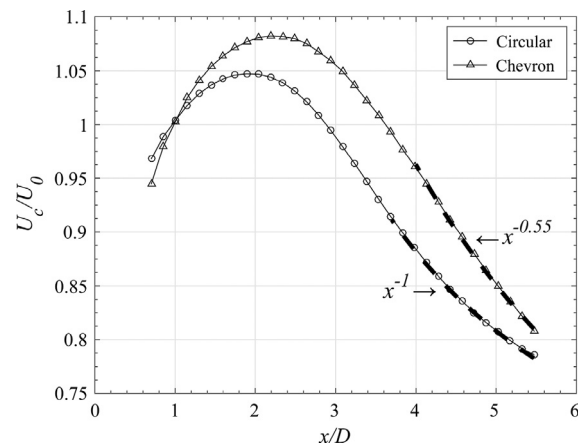
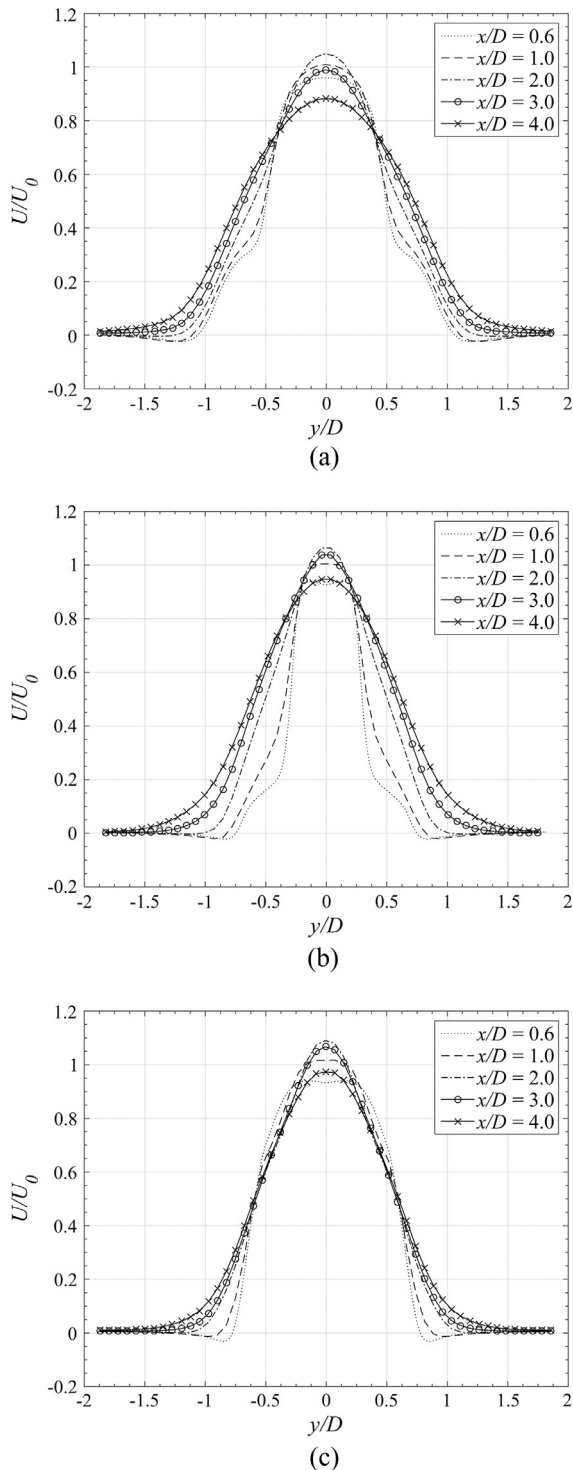


Fig. 3. Time-averaged axial velocity component along the jet centreline ( $U_c$ ) for the circular and the chevron synthetic jets.



**Fig. 4.** Spatial distribution of  $U$  in the  $y$ -direction at  $x/D = 0.6, 1.00, 2.00, 3.00, 4.00$ . (a) Circular synthetic jet, (b) apex and (c) notch of the chevron synthetic jet.

and the negative  $U$  are not detected anymore. From  $x/D \geq 2$ ,  $U$  shows the same bell-shaped distribution as for the circular exit.

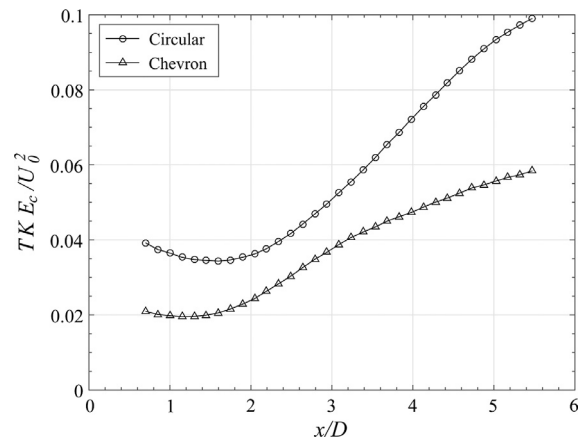
In the notch plane, the jet is issued from a larger exit area with same radius of the circular exit. The  $U$  profile at  $x/D = 0.6$  is wider than that of the circular configuration. Similar to the apex plane, a region characterized by negative  $U$  is present and two small peaks can be observed at  $y/D = \pm 0.2$ . In this case, the lateral slope does not change (Fig. 4c) and this can be addressed to the average lateral transport of high momentum fluid at the notch [36].

Fig. 5 shows the turbulent kinetic energy behaviour along the jet centreline ( $TKE_c$ ). The chevron jet lowers the turbulence intensity along the jet centreline, in agreement with Violato and Scarano [25]. The trend of the  $TKE_c$  is similar for both configurations showing a reduction followed by an increase. The increase of the  $TKE_c$  for the circular synthetic jet is much stronger than that for the chevron one reaching approximately twice the intensity at  $x/D = 5.5$ .

Contours of  $TKE$  in the  $x$ - $y$  plane are reported in Fig. 6. At  $x/D = 0.6$ , the circular exit (Fig. 6a) shows two local maxima at  $y/D = \pm 0.5$  (inner high turbulent region) and  $y/D = \pm 0.85$  (outer high turbulent region). The peak of  $TKE$  in the outer turbulent region is caused by the turbulence production in the vortexring core, while in the inner turbulent region is due to the shear layer between the trailing jet and the external quiescent ambient. At more downstream locations, the inner and outer turbulent regions merge because of the spreading of both the high turbulent region and of the shear layer. For both configurations, a low intensity  $TKE$  region is measured across the centreline (i.e., inner region) in the near field corresponding to the jet width reduction. Downstream of this low turbulent intensity region, the  $TKE$  increases and the high turbulent intensity area spreads because of the growth of the turbulent vortex ring [37].

Focusing on the chevron synthetic jet, the  $TKE$  maps (Fig. 6b for the apex plane and Fig. 6c for the notch plane) show that, near the nozzle exit, the high turbulent region is respectively tighter and thicker than the one of the circular jet. In the apex plane, the outer turbulent region is barely visible and, the high turbulence intensity is measured in the shear layer. Differently in the notch plane, the high  $TKE$  area is thicker because of the presence of both the shear layer and the vortex ring. At more downstream locations, for both planes the high turbulent region spreads and the  $TKE$  intensity decreases. On the other hand, a small increase of  $TKE$  is measured at the end of the FOV. For  $1.5 < x/D < 4.5$ , the turbulence intensity decreases and the turbulence generated by the shear layer prevails over the one related to the vortex ring. At more downstream location this trend is reversed by the prevailing vortex ring effect.

Comparing the  $TKE$  intensity levels for the two devices, the chevron nozzle shows larger intensity in the near field ( $x/D < 1.5$ ), while lower intensity at more downstream locations. These findings are in agreement with previous literature on continuous chevron jets [38,39]. This calming effect, as named by Zaman et al. [20] for continuous jets, may be a consequence of the stream-wise vortices, which reduce the turbulence in the shear layer. These aspects will be clearly analysed in the following section.



**Fig. 5.**  $TKE$  along the jet centreline ( $TKE_c$ ) for the circular and the chevron synthetic jets.

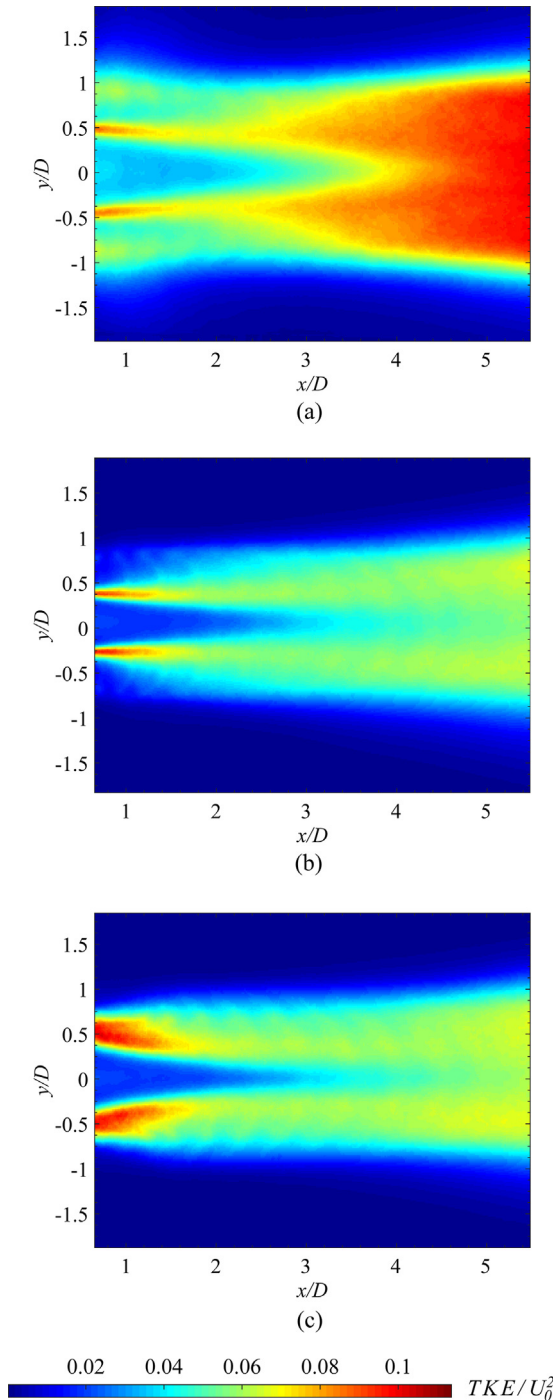


**Fig. 6.** Time-averaged  $TKE$  maps for (a) circular, (b) apex and (c) notch planes.

### 3.2. Phase-averaged velocity field

The phase evolution of the two synthetic jets is discussed by looking at both the phase-averaged mean velocity and  $\langle TKE \rangle$  fields. The phase evolution of the circular synthetic jet is reported in the first column of Fig. 7 where the phase-locked axial ( $\langle u \rangle$ ) and the radial ( $\langle v \rangle$ ) velocity components are reported in the top and bottom part of each subplot. The vortex ring, visualized through the projection of the velocity vectors in the  $x$ - $y$  plane, is fully visible in the measurement area at  $\phi = 60^\circ$ . In the jet core, i.e. the area embedded between the vortex ring, the  $\langle u \rangle$  is approximately constant in the  $y$ -direction up to  $0.5 D$  from the jet axis. At  $\phi = 120^\circ$ ,

the region of high  $\langle u \rangle$  is still embedded within the vortex ring but its intensity decreases. Moreover, in the wake of the vortex ring, the trailing jet is formed. The vortex ring reduces its intensity convecting downstream as suggested by the maps of the axial and radial velocity components. During the last phase of ejection, the trailing jet is weakly visible and the spanwise velocity profile within the trailing jet is bell shaped.

The phase-locked evolution of the chevron synthetic jet is reported in the second and third column of Fig. 7 for the apex and notch plane, respectively. Starting from  $\phi = 60^\circ$ , the phase at which the vortex ring is fully visible, it is evident that in the apex plane at  $x/D = 0.6$  the spanwise extension of the region where  $\langle u \rangle / U_0 \geq 75\%$ , is approximately 30% narrower than for the circular configuration. On the other hand, along the notch plane the spanwise extension of this region is approximately 20% larger than for the circular configuration. At this phase, at approximately  $0.2 < y/D < 0.4$ , close to the jet core, the radial velocity component shows a motion towards the jet axis in the apex plane and an opposite motion, away from the jet axis, in the notch plane. These flow components are induced by streamwise vortices generated at the root of the chevron teeth (as discussed in the next section). Increasing  $\phi$ , the strength of both the inward and outward motions reduces because of the weaker streamwise vortices. At  $\phi = 120^\circ$ , small differences in the  $\langle v \rangle$  component are measured at the trailing jet location (see circle in Fig. 7). Both axial and radial velocity maps suggest a wider shear layer characterized by outflow along the notch plane and a tighter shear layer characterized by inflow along apex plane. At  $\phi = 168^\circ$ , no appreciable difference between the two planes of the chevron jet is detected.

The statistical flow properties are discussed by looking at  $\langle TKE \rangle$ , illustrated in Fig. 8. For the circular configuration, at  $\phi = 60^\circ$  local high turbulence intensity regions are detected in the vortex-ring core and across the shear layer between the jet core and the vortex ring. As the vortex ring moves downstream ( $\phi = 120^\circ$ ), the  $\langle TKE \rangle$  in the vortex core increases and the area of high turbulence intensity becomes wider. The trailing jet is characterized by a high  $\langle TKE \rangle$  intensity region across the shear layer near the nozzle exit. Further downstream, at  $\phi = 168^\circ$ , the  $\langle TKE \rangle$  across the trailing jet decreases its intensity while the region of high  $\langle TKE \rangle$  inside the vortex ring core spreads towards the jet axis.

The chevron synthetic jet shows a completely different phase evolution of the  $\langle TKE \rangle$ . At  $\phi = 60^\circ$ , along the apex plane local maxima of  $\langle TKE \rangle$  are observed in the vortex-ring core and in the region between the jet core and the vortex ring. Oppositely, in the notch plane the two regions cannot be distinguished. At  $\phi = 120^\circ$ , the  $\langle TKE \rangle$  intensity is approximately the same in both the core of the vortex ring and along the trailing jet. Differently, the circular configuration shows high turbulence fluctuations intensity in the vortex core region. This uniformity in the intensity of the  $\langle TKE \rangle$  is due to the redistribution of the turbulent kinetic energy between the two large structures present in the chevron configuration: streamwise vortices and non-circular vortex ring (as it will be shown in the next section). When the vortex convects downstream, at  $\phi = 168^\circ$ , the differences between the apex and the notch planes disappear. Furthermore, at this phase, the chevron synthetic jet shows only one region with relatively high  $\langle TKE \rangle$  near the vortex ring core whose values are definitely lower than those present in the circular configuration.

The difference in the spatial and time evolution of the  $\langle TKE \rangle$  may be explained by looking at the formation and evolution of the coherent structures, which are reported in the next section. The circular synthetic jet is characterized by a larger turbulence intensity in the vortex-ring core than along the shear layer of the trailing jet. These regions may be caused by the roll-up of the vortex ring and by the shear layer generated at the interface between the jet column and the surrounding environment. At

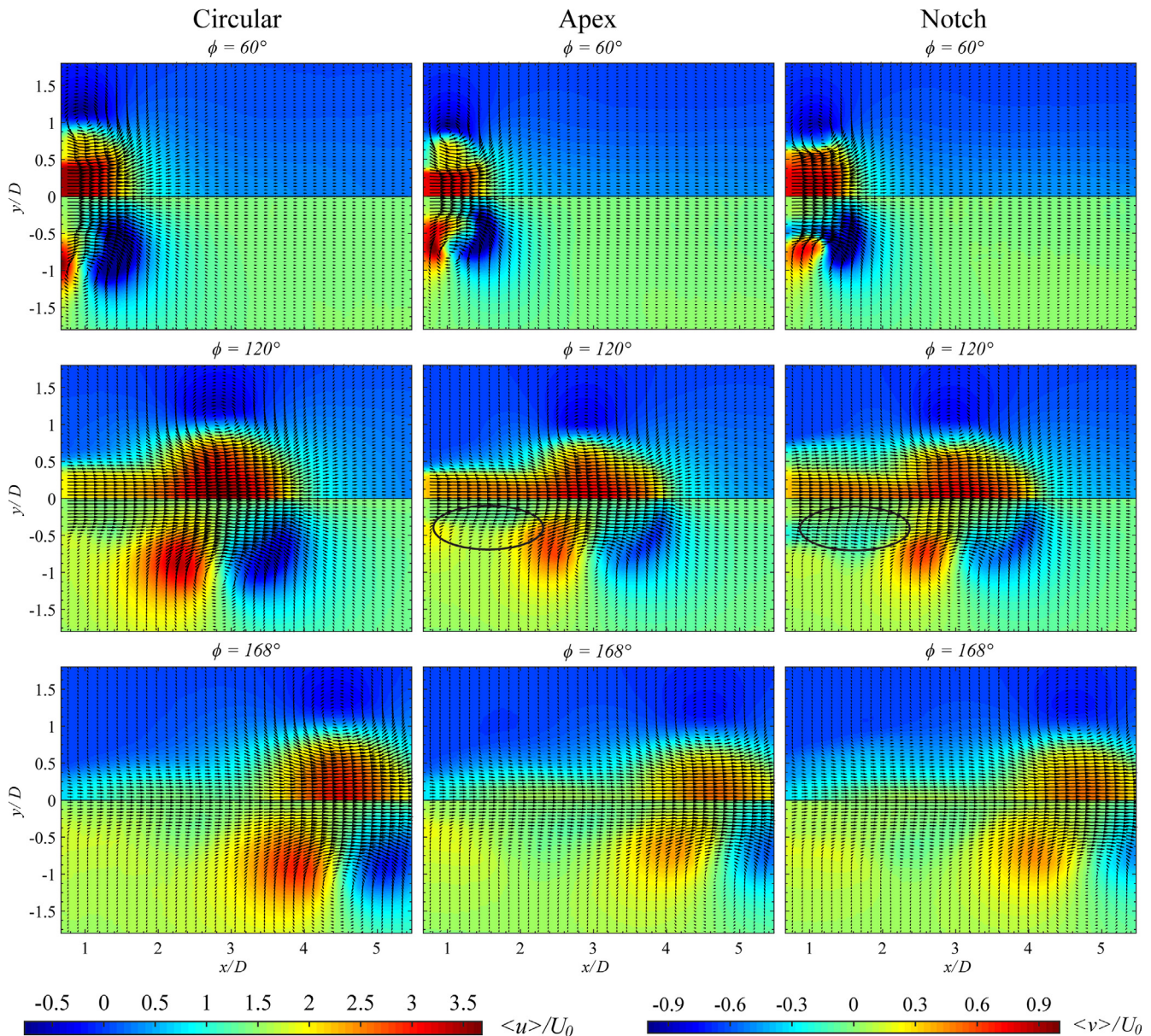


**Fig. 7.** Phase-averaged axial (top) and radial (bottom) velocity components maps for circular (first column) and chevron (apex plane in the second column and notch plane in the third column) synthetic jets.

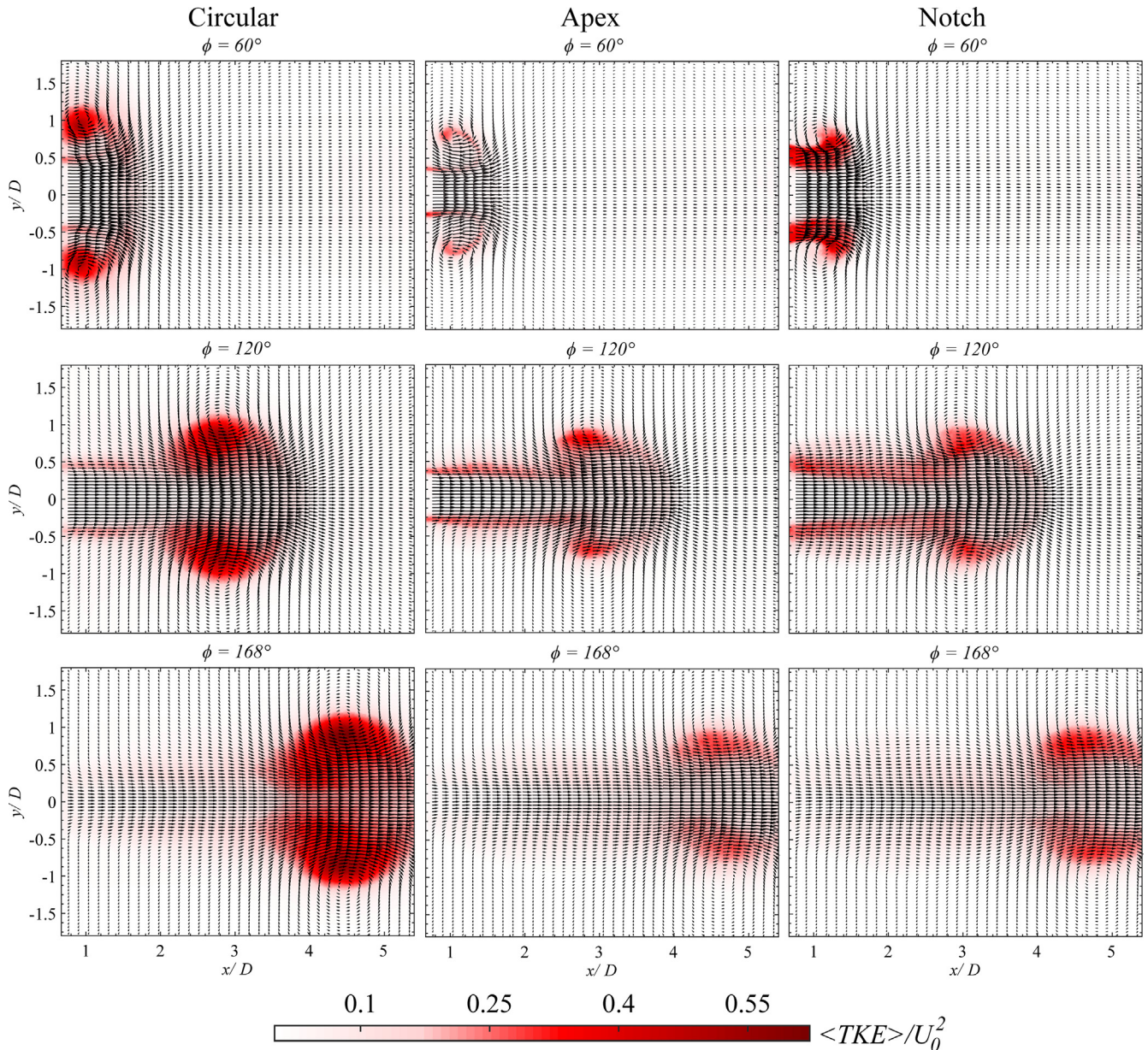
more downstream locations (subsequent  $\phi$ ), the vortex ring dissipates generating a wider and higher turbulence intensity area [37]. Differently, the chevron synthetic jet is characterized by both streamwise and azimuthal vortices, as reported in Fig. 12. The formation of the streamwise structures at the notches may explain the larger intensity of the  $\langle TKE \rangle$  at this location. Differently from the circular case, at more downstream locations, the  $\langle TKE \rangle$  is less intense in the vortex-ring core but slightly more intense along the trailing jet. This may be ascribed to the vorticity redistribution. As a matter of fact, the vorticity dissipates both along the trailing jet and the vortex ring-core, resulting in the measured  $\langle TKE \rangle$  pattern. The streamwise vorticity appears to reduce the turbulence intensity of the vortex ring compared to the circular case. A similar effect was found by Zaman et al. [20] for continuous chevron jet.

Fig. 9 reports the  $x$ - $y$  location per phase of the vortex-ring core generated in presence of the chevron nozzle exit along the apex and notch planes. The vortex-ring core location is detected as the location of maximum intensity of out-of-plane vorticity ( $\omega_z$ ). In

the figure, data for  $\phi < 24^\circ$  are not reported because the vortex ring is not fully present in the FOV. During the phase-evolution ( $48^\circ \leq \phi < 168^\circ$ ) the position of vortex-ring core in the apex plane is always farther from the jet axis and closer to the nozzle exit with respect to the notch plane. The distance reduces at the following phases and at  $\phi = 168^\circ$  both the  $x$  and  $y$  positions merge. This is due to the fact that the vortex ring of the chevron synthetic initially assumes a non-circular shape while, at a more downstream location, it tends to a classic circular vortex ring shape, as will be shown in the next section.

### 3.3. 3D reconstructions

In order to study the three-dimensional flow organization for the two investigated configurations, the flow field is reconstructed by means of scanning Stereo-PIV measurements for three phases corresponding to  $\phi = 84^\circ$ ,  $120^\circ$  and  $168^\circ$ .



**Fig. 8.** Phase-averaged turbulent kinetic energy maps for circular (first column) and chevron (apex plane in the second column and notch plane in the last column) synthetic jets.

The circular synthetic jet is characterized by a vortex ring (Fig. 10) that becomes weaker moving downstream as already discussed in the previous section and reported in the literature [16,17]. As a matter of fact, by using the  $Q$  criterion [40] to visualize the vortices, two different iso-surface levels equal to 25 and 15 are used to visualize the same vortex structure at  $\phi = 120^\circ$  and  $168^\circ$ , respectively.

More interesting is the flow pattern of chevron synthetic jet. The effect of the chevron teeth is to re-orient the azimuthal vorticity into streamwise vorticity ( $\omega_x$ ) [25] with consequent formation of streamwise oriented counter-rotating vortices, six for the investigated nozzle configuration, generated at the notches of the chevron exit (Fig. 11a). These counter-rotating vortices induce extra flow motions towards the jet axis and far from the jet axis in correspondence of the notches and the apices respectively, as previously discussed. As a consequence, both the trailing jet and the vortex ring show a modified shape with respect to the conventional circular pat-

tern. As a matter of fact, by looking at the cross-plane at  $x/D = 1.75$  for  $\phi = 84^\circ$  (Fig. 11b), the vortex ring is azimuthally modulated, as visualized through the iso-line of  $Q$ . The streamwise vortices induce opposite vorticity within the vortex ring as shown in Fig. 11b. The presence of appreciable values of  $\omega_x$  within a vortex ring may induce the phenomenon of the axis-switching [22]. However, the mutual interaction between streamwise and azimuthal prevents the self-deformation of the vortex ring in agreement with Zaman [23]. For this reason, the vortex ring convects downstream keeping unchanged its topology up to  $\phi = 120^\circ$  (where the vortex ring core is at approximately  $x/D = 3$  from the nozzle exit). At a later stage of the ejection phase, both the streamwise vortices and the vortex ring become weaker; when the streamwise oriented counter-rotating vortices disappear ( $\phi = 168^\circ$ ) the vortex ring shows a circular shape (Fig. 12b). The evolution reflects the behaviour of non-circular jet to develop into an axisymmetric structure, as also seen by Gutmark and Grinstein [41].

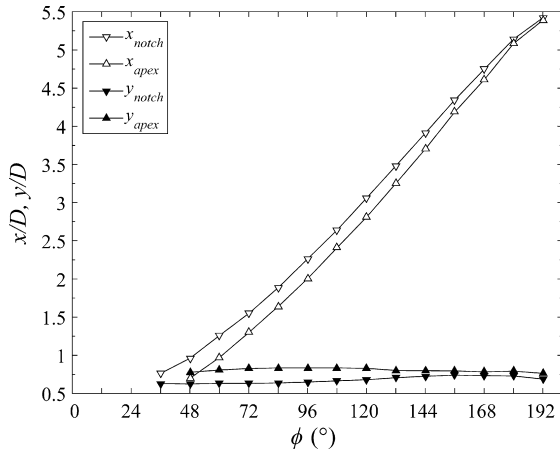


Fig. 9. Streamwise ( $x$ ) and radial ( $y$ ) location of the vortex ring core along the apex and notch planes.

#### 4. Conclusions

The circular and chevron synthetic jets flow field has been experimentally studied by means of Stereo-PIV.

The comparison of the time-average behaviour between the chevron and the circular flow field shows that the former is characterized by a higher axial velocity along the jet axis with maximum located  $0.4 D$  more downstream. After the velocity peak, the mean velocity along the axis decreases differently between the two configurations: as  $x^{-1}$  for the circular jet, and  $x^{-0.55}$  for the chevron one. The chevron synthetic jet shows two different behaviours in the apex and notch planes. Indeed, the time-averaged axial velocity component profile in the apex plane has a width smaller than the circular synthetic jet, while in the notch plane it is larger. Furthermore, the change of the lateral slope in the spanwise profile is present in the apex plane while is not visible in the notch plane. At  $x/D > 3$ , the profiles along the two planes are similar and the spanwise profile of the axial velocity is bell-shaped as for the circular jet.

The time-averaged *TKE* distribution presents local maxima in correspondence of the vortex ring and of the shear layer between the trailing jet and the external quiescent ambient. For the circular synthetic jet, *TKE* intensity associated with the vortex ring is larger than the one associated with the shear layer. An opposite behaviour is measured in presence of the chevron synthetic jet. Moreover, for  $x/D > 1.5$ , the chevron exit generates a jet with lower *TKE* intensity with respect to the circular one.

The different exit shape strongly affects the topology of the coherent vortex structures present in the flow field. In the circular

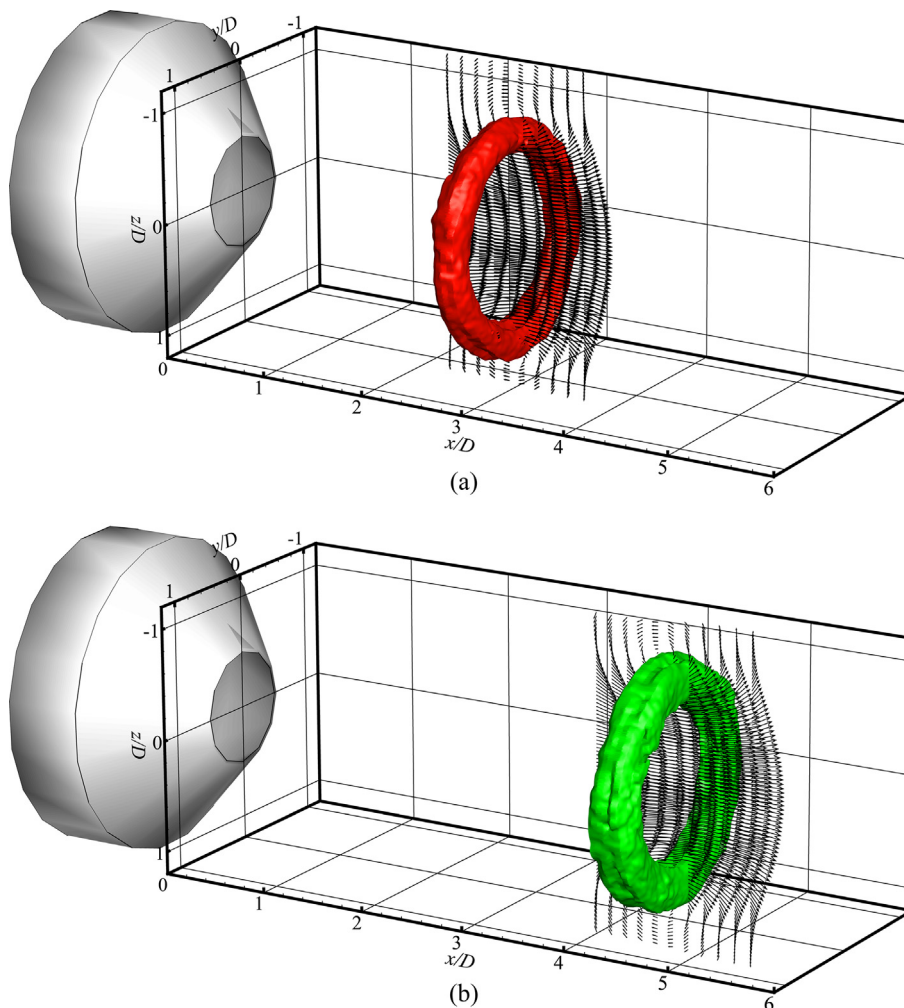
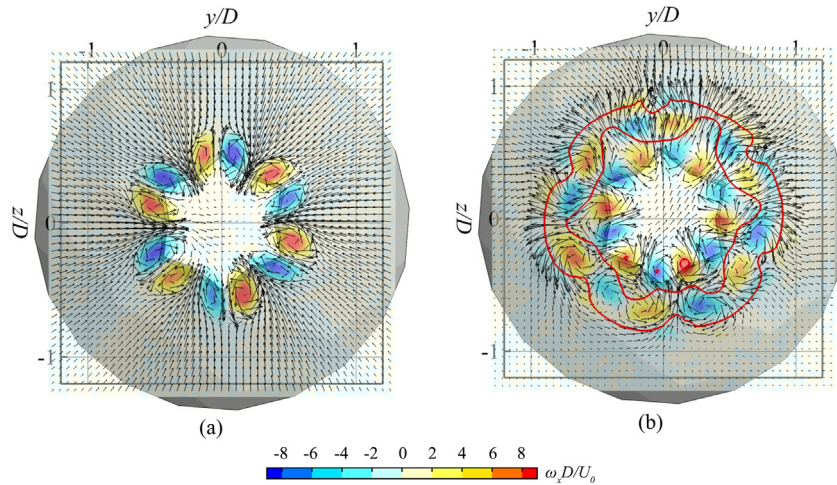
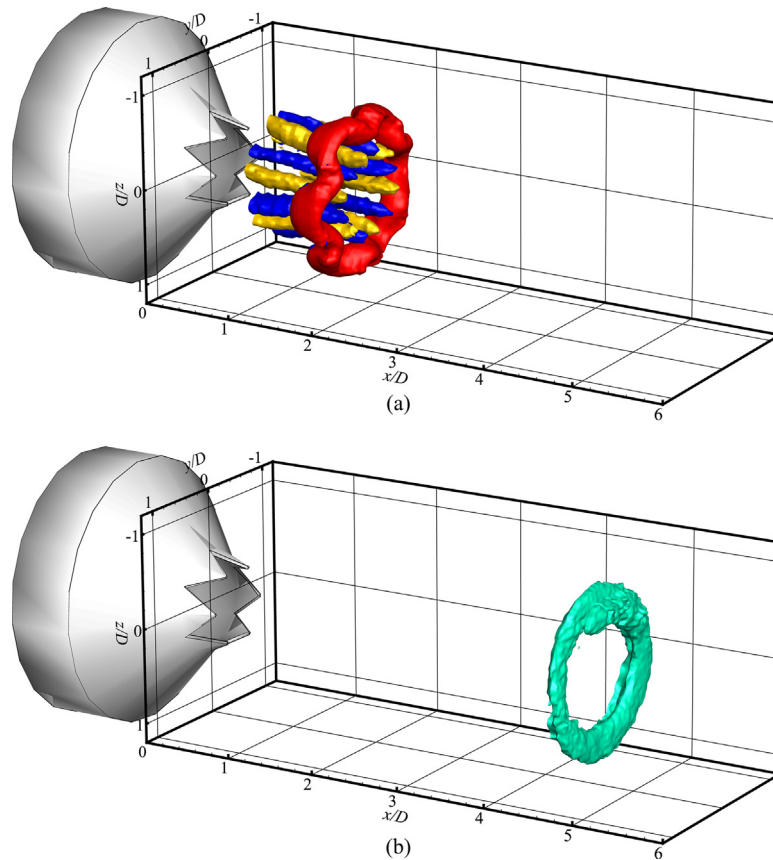


Fig. 10. Three-dimensional reconstruction of the flow field at phase (a)  $120^\circ$  and (b)  $168^\circ$  for circular synthetic jet. Red iso-surface with  $QD^2/U_0^2 = 25$  and green iso-surface with  $QD^2/U_0^2 = 15$ .



**Fig. 11.** Crosswise slice at (a)  $x/D = 1$  and (b)  $x/D = 1.75$  at  $\phi = 84^\circ$  with  $\omega_x$  maps and red solid iso-lines of  $QD^2/U_0^2 = 35$ .



**Fig. 12.** Three-dimensional reconstruction of the coherent vortex structures at  $\phi$  equal to (a)  $84^\circ$  and (b)  $168^\circ$  for chevron synthetic jet  $QD^2/U_0^2$  iso-surface equal to 35 (red one) and 10 (light blue one) and  $\omega_x$  iso-surfaces equal to  $-4$  (blue ones) and  $4$  (yellow ones) are represented. (For interpretation of the references to color in this figure legend, the reader is referred to the web version of this article.)

configuration, the flow field is only characterized by a vortex ring convecting downstream. This vortex structure dissipates its energy moving downstream generating high intensity *TKE* regions that penetrates towards the jet axis. Differently, the chevron synthetic jet configuration presents a more complex flow field characterized by streamwise vortices that alter the shape of the vortex ring. However, the mutual interaction between the coherent structures avoids the onset of the axis-switching phenomenon. During its evolution, for  $x/D > 3$ , the streamwise vortices disappear and the

azimuthal coherent vortex structure assumes a circular shape. Differently from the circular configuration, the *TKE* intensity generated by the vortex ring decreases as it convects downstream.

#### Acknowledgements

The authors kindly acknowledge Delft University of Technology and prof. F. Scarano for providing the contoured nozzle and the

chevron exit. Furthermore, the authors wish to thank Mrs. Laura Vitale for the support during the preliminary experimental tests.

## References

- [1] R. Raju, R. Mittal, L. Cattafesta, Dynamics of airfoil separation control using zero-net mass-flux forcing, *AIAA J.* 42 (12) (2008) 3103–3115.
- [2] N.A. Buchmann, C. Atkinson, J. Soria, Influence of ZNMF jet flow control on the spatio-temporal flow structure over a NACA-0015 airfoil, *Exp. Fluids* 54 (3) (2013) 1–14.
- [3] D. Smith, M. Amitay, V. Kibens, D. Parekh, A. Glezer, Modification of lifting body aerodynamics using synthetic jet actuators, *AIAA Paper*, vol. 209, 1998.
- [4] M. Amitay, D.R. Smith, V. Kibens, D.E. Parekh, A. Glezer, Aerodynamic flow control over an unconventional airfoil using synthetic jet actuators, *AIAA J.* 39 (3) (2001) 361–370.
- [5] B.L. Smith, A. Glezer, Jet vectoring using synthetic jets, *J. Fluid Mech.* 39 (3) (2002) 1–34.
- [6] M. Chaudhari, B. Puranik, A. Agrawal, Effect of orifice shape in synthetic jet based impingement cooling, *Exp. Thermal Fluid Sci.* 34 (2) (2010) 246–256.
- [7] M. Chaudhari, B. Puranik, A. Agrawal, Heat transfer characteristics of synthetic jet impingement cooling, *Int. J. Heat Mass Transf.* 53 (5) (2010) 1057–1069.
- [8] T. Persoons, A. McGuinn, D.B. Murray, A general correlation for the stagnation point Nusselt number of an axisymmetric impinging synthetic jet, *Int. J. Heat Mass Transf.* 54 (17) (2011) 3900–3908.
- [9] R. Mahalingam, A. Glezer, Design and thermal characteristics of a synthetic jet ejector heat sink, *J. Electron. Packag.* 127 (2) (2005) 172–177.
- [10] C.S. Greco, A. Ianiro, G. Cardone, Time and phase average heat transfer in single and twin circular synthetic impinging air jets, *Int. J. Heat Mass Transf.* 73 (2014) 776–788.
- [11] Q. Gallas, R. Holman, T. Nishida, B. Carroll, M. Sheplak, L. Cattafesta, Lumped element modeling of piezoelectric-driven synthetic jet actuators, *AIAA J.* 41 (2) (2003) 240–247.
- [12] T. Persoons, General reduced-order model to design and operate synthetic jet actuators, *AIAA J.* 50 (4) (2012) 916–927.
- [13] L. de Luca, M. Girfoglio, G. Coppola, Modeling and experimental validation of the frequency response of synthetic jet actuators, *AIAA J.* 52 (8) (2014) 1733–1748.
- [14] R. Holman, Y. Utturkar, R. Mittal, B.L. Smith, L. Cattafesta, Formation criterion for synthetic jets, *AIAA J.* 43 (10) (2005) 2110–2116.
- [15] A. McGuinn, R. Farrelly, T. Persoons, D.B. Murray, Flow regime characterisation of an impinging axisymmetric synthetic jet, *Exp. Thermal Fluid Sci.* 47 (2013) 241–251.
- [16] B.L. Smith, A. Glezer, The formation and evolution of synthetic jets, *Phys. Fluids* 10 (9) (1998) 2281–2297.
- [17] J.E. Cater, J. Soria, The evolution of round zero-net-mass-flux jets, *J. Fluid Mech.* 472 (2002) 167–200.
- [18] B.L. Smith, G.W. Swift, A comparison between synthetic jets and continuous jets, *Exp. Fluids* 34 (4) (2003) 467–472.
- [19] K. Jambunathan, E. Lai, M.A. Moss, B.L. Button, A review of heat transfer data for single circular jet impingement, *Int. J. Heat Fluid Flow* 13 (2) (1992) 106–115.
- [20] K.B.M.Q. Zaman, J. Bridges, D. Huff, Evolution from ‘tabs’ to ‘chevron technology’ – a review, *Int. J. Aeroacoustics* 10 (5–6) (2011) 685–710.
- [21] D. Violato, A. Ianiro, G. Cardone, F. Scarano, Three-dimensional vortex dynamics and convective heat transfer in circular and chevron impinging jets, *Int. J. Heat Fluid Flow* 37 (2012) 22–36.
- [22] F.F. Grinstein, E.J. Gutmark, T.P. Parr, D.M. Hanson-Parr, U. Obeysekare, Streamwise and spanwise vortex interaction in an axisymmetric jet. A computational and experimental study, *Phys. Fluids* 8 (6) (1996) 1515–1524.
- [23] K.B.M.Q. Zaman, Axis switching and spreading of an asymmetric jet: the role of coherent structure dynamics, *J. Fluid Mech.* 316 (1996) 1–27.
- [24] I.A. Waitz, Y.J. Qiu, T.A. Manning, A.K.S. Fung, J.K. Elliot, J.M. Kerwin, J.K. Krasnodebski, M.N. O’Sullivan, D.E. Tew, E.M. Greitzer, F.E. Marble, C.S. Tan, T. G. Tillman, Enhanced mixing with streamwise vorticity, *Prog. Aerosp. Sci.* 33 (5) (1997) 323–351.
- [25] D. Violato, F. Scarano, Three-dimensional evolution of flow structures in transitional circular and chevron jets, *Phys. Fluids* 23 (12) (2011) 124104.
- [26] M. Raffel, C.E. Willert, J. Kompenhans, *Particle Image Velocimetry: A Practical Guide*, Springer, 2013.
- [27] C.S. Greco, A. Ianiro, T. Astarita, G. Cardone, On the near field of single and twin circular synthetic air jets, *Int. J. Heat Fluid Flow* 44 (2013) 41–52.
- [28] T. Astarita, G. Cardone, Analysis of interpolation schemes for image deformation methods in PIV, *Exp. Fluids* 38 (2) (2005) 233–243.
- [29] T. Astarita, Analysis of interpolation schemes for image deformation methods in PIV: effect of noise on the accuracy and spatial resolution, *Exp. Fluids* 40 (6) (2006) 977–987.
- [30] T. Astarita, Analysis of weighting windows for image deformation methods in PIV, *Exp. Fluids* 43 (6) (2007) 859–872.
- [31] T. Astarita, Analysis of velocity interpolation schemes for image deformation methods in PIV, *Exp. Fluids* 45 (2) (2008) 257–266.
- [32] J. Westerweel, F. Scarano, Universal outlier detection for PIV data, *Exp. Fluids* 39 (6) (2005) 1096–1100.
- [33] A. Hussain, W. Reynolds, The mechanics of an organized wave in, *J. Fluid Mech.* 41 (02) (1970) 241–258.
- [34] S.G. Mallinson, G. Hong, J.A. Reizes, Some characteristics of synthetic jets, *AIAA Paper*, vol. 3651, 1999.
- [35] G.N. Abramovich, *The Theory of Turbulent Jets*, The Massachusetts Institute of Technology Press, Cambridge, 1963.
- [36] S.S. Pannu, N.H. Johannesen, The structure of jets from notched nozzles, *J. Fluid Mech.* 74 (03) (1976) 515–528.
- [37] T. Maxworthy, Some experimental studies of vortex rings, *J. Fluid Mech.* 81 (03) (1977) 465–495.
- [38] M.J. Doty, B.S. Henderson, K.W. Kinzie, Turbulence measurements of separate-flow nozzles with pylon interaction using particle image velocimetry, *AIAA J.* 45 (6) (2007) 1281–1289.
- [39] J. Bridges, M.P. Wernet, Turbulence measurements of separate flow nozzles with mixing enhancement features, *AIAA Paper*, vol. 2484, no. 0704–0188, 2002.
- [40] J. Jeong, F. Hussain, On the identification of a vortex, *J. Fluid Mech.* 285 (1995) 69–94.
- [41] E.J. Gutmark, F.F. Grinstein, Flow control with noncircular jets, *Annu. Rev. Fluid Mech.* 31 (1) (1999) 239–272.